1 **Neutral and Dicationic [5]helicene-embedded Cycloparaphenylene**

2 **Nanohoops with Möbius Topology and Local/In-Plane Aromaticity**

3 Huiji Yang, Shengzhu Guo, Weijie Guo, Lin Liu, Xiaoyu Liu, Jing He, Yanqing

4 Fan, Zhe Lian, Xiaonan Li, Shu Huang, Xuebo Chen, Ying Wang,* and Hua

5 Jiang*

6 *College of Chemistry, Beijing Normal University, Beijing 100875 (P. R. China).*

7 **KEYWORDS.** Möbius topology, aromaticity, nanohoop, helicene, circularly

8 polarized luminescence

9 **ABSTRACT:** The relationship between Möbius topology and aromaticity is still

10 elusive to date, which is, to a large extent, due to the related synthetic

11 challenges and, further, the scarcity in both the quantity and the diversity of the

12 constructed Möbius systems. In this work, we report the synthesis of [4n]Möbius

13 conjugated all-carbon nanohoops (**[5]H-[7,8]CPPs**) by utilizing a [5]helicene

14 unit as a hidden writhe and a masked aromatic unit to overcome the strain

15 inherited from Möbius topology. X-ray analyses reveal that **[5]H-[7,8]CPPs**

16 contain a [5]helicene moiety and an oligoparaphenylene unit, and display a

17 Möbius topology. Photophysical investigations demonstrated that **[5]H-**

18 **[7,8]CPPs** exhibited moderately high fluorescence quantum yields, which are

19 significantly higher than those of pristine [5]helicene and [7,8]CPPs. Chiroptical

20 studies revealed that **[5]H-[7,8]CPPs** displayed an obvious Cotton effect in

21 circular dichroism and bright circularly polarized luminescence, indicating that

22 the chirality of [5]helicene was efficiently transferred to the overall carbon

23 nanohoops. Importantly, theoretical investigations reveal that, though

24 possessing a Möbius topology and a 4n π-electron array in the neutral state,

25 such all-carbon nanohoops fundamentally exhibit local Hückel aromaticity,

26 while their dications, with a 4n+2 π-electron in the conjugation circuits, show

27 Hückel in-plane global aromaticity, deviating from the Heilbronner prediction.

28 The results may help us to better understand the complicated relationship

29 between Möbius topology and aromaticity.

Introduction

31   The research on aromaticity and stability of cyclic π-conjugated systems

32 with distinct topology has attracted much attention of both organic and theoretic

33 chemists, and received a significant evolution in synthesis and theory since the

34 landmark discovery of benzene by Faraday in 1825. [1-5] It is well recognized that

35 annulenes displaying a Hückel topology are aromatic and stable when their

36 cyclic conjugated π-electrons are 4n+2, whereas those with 4n are antiaromatic

37 and unstable. However, when annulene is twisted by 180° to adopt a Möbius

38 topology that is the classic example of a non-orientable surface, its electronic

39 structure and aromatic character were changed significantly. The concept of

40 Möbius aromaticity, proposed by Heilbronner in 1964, predicted that Möbius

41 annulenes with 4n conjugated π-electrons should be aromatic and stable. [6]

42 Since then, annulenes with a Möbius topology have aroused tremendous

43　interest to both synthetic organic and theoretic chemists. One of important

44　milestones in the field of Möbius aromaticity was demonstrated by the first

45　successful synthesis of a [16] Möbius annulene by Herges and co-workers in

46　2003, [7] and followed by the expanded porphyrin with a dynamic Möbius-Hückel

47　aromaticity. [8] After that, the topic of Möbius aromaticity has been mainly

48　dominated by expanded porphyrinoid systems because their structural features

49　can potentially stabilize Möbius aromatic systems. [9-11]

50　　　Stimulated by recent advances on all-carbon macrocycle-based

51　nanoarchitectures such as catenanes and knots, [12-21] conjugated all-carbon

52　nanohoops with a Möbius topology have recaptured great attention of scientists

53　from synthetic organic chemistry, physical science and material science. So far,

54　there are limited examples of Möbius conjugated all-carbon nanohoops

55　because of the synthetic difficulties associated with the twisted topological

56　structure. [3-5] In 2014, Herges and co-workers reported the first triply twisted

57　Möbius [24]dehydroannulene, [22] whose conjugation is interrupted by large

58　torsional angles due to its flexible building blocks. Durola and Herges then

59　developed a triple cyclic tri-[5]helicenes with a Möbius topology, exhibiting a

60　strong diatropic ring current in the outer periphery. However, no net macrocyclic

61　aromaticity was displayed due to the counterbalance of the diatropic and

62　paratropic currents in the outer π and the inner σ system, respectively. [23] Moore

63　and co-workers reported the synthesis of a Möbius tris((ethynyl)[5]helicene)

64 macrocycle without obvious global aromaticity due to the weak conjugation

65 between the alkyne and adjacent helicene units. [24] Cong and Zhu disclosed the

66 aromaticity of mechanically interlocked Möbius conjugated nanohoops. [25]

67 Šolomek reported a Möbius nanohoop containing [6]helicene unit with circularly

68 polarized luminescence, but without global Möbius aromaticity because the

69 presence of [6]helicene in nanohoop leads to an odd number of π-electrons in

70 the cyclic conjugated pathway. [26] Very recently, a Möbius topology has been

71 disclosed in the twisted [n]cycloparaphenylenes ([n]CPPs) with alkene insertion

72 by Kayahara and Yamago. [27] Besides above excellent advances, there are a

73 few elegant examples on other aromatic macrocycles with a Möbius topology.

74 [28-33] Nevertheless, the relationship between Möbius topology and

75 aromaticity/chirality, in particular if there is inevitable connection between

76 [4n]Möbius topology and Möbius aromaticity, is still far from being fully

77 understood.

78 We have a long-term interest in conjugated carbon nanohoops [34-39]. In

79 particular, we are very interested in the fabrication of highly π-conjugated

80 nanohoops with well-defined Möbius topologies and, at the same time,

81 passionately curious about the relationship between the topology/electronic

82 structure and the aromaticity for such systems.[6] Herein, we present the design

83 and synthesis of [4n]Möbius conjugated all-carbon nanohoops (**5[H]-[7,8]CPPs**,

84 Figure 1 and Scheme 1) by combining [5]helicene and cycloparaphenylenes.

85 We demonstrated that the presence of [5]helicene unit in

86 [7,8]cycloparaphenylenes enables the conjugated all-carbon nanohoops to

87 exhibit a distinct Möbius topology as demonstrated by X-ray crystal structures

88 and bright circularly polarized luminescence. More interestingly, DFT

89 computations indicate that the neutral nanohoops, **5[H]-[7,8]CPPs**, are local

90 Hückel-aromatic systems, while the corresponding dicationic ones, which

91 possess 4n+2 π-electrons in the conjugation circuits, exhibit in-plane global

92 aromaticity, as revealed by the structural analyses as well as the results of

93 Nucleus-independent chemical shifts (NICS/2D-NICS), Anisotropy of the

94 induced current density (AICD) and localized orbital locator-π/σ (LOL-π/σ)

95 calculations. Our observations apparently deviate from that Heilbronner

96 predicted, implying that the relationship between the topology/electronic

97 structure and the aromaticity might be diverse for different π-conjugated Möbius

98 systems.

99 **Design and Synthesis**

100 In a singly twisted Möbius annulene featuring a molecular twist and an

101 overall macrocyclic conjugation (Figure 1), a 180° twist induces strain in π-

102 conjugated macrocycle and thus causes tremendous difficulties in stabilizing

103 the Möbius topology. The utilization of a hidden writhe such as helicene to

104 circumvent this difficulty has been successfully demonstrated in helicene-based

105 Möbius annulenes. [23, 24, 26] However, this method is not yet enough to mitigate

106 strain caused by the overall macrocyclic conjugation within a singly twisted

107 Möbius annulene. On the other hand, a 3,6-*syn*-dimethoxy-cyclohexa-1,4-diene

108 moiety as a masked aromatic ring has been successfully used to develop

109 strained [n]cycloparaphenylenes ([n]CPPs) followed by sequential

110 aromatization. [40]
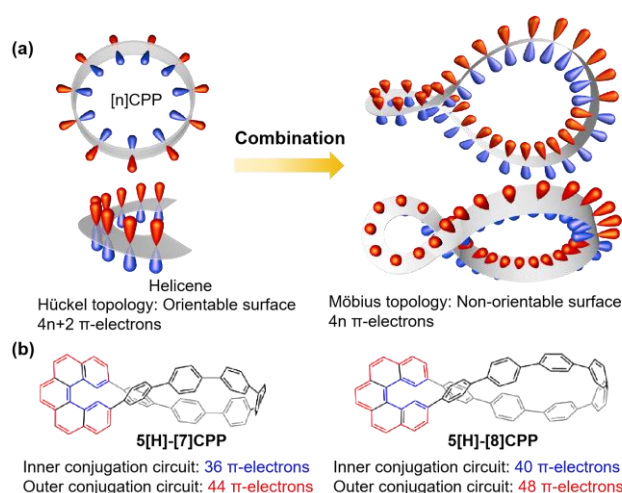
Figure 1. Concept of this work. (a) The cartoon illustration of hybridization of two conjugated subunits ([5]helicene and CPP) with a Hückel topology into a globally conjugated carbon nanohoop with a Möbius topology. (b) the structures of the [4n]Möbius conjugated all-carbon nanohoops studied herein. Each nanohoop contains two different conjugated circuits dependent on the inner (blue) or outer (red) paths of helicene. All cyclic conjugation paths contain 4n π-electrons.

117 The cyclohexadiene moiety could be utilized to construct marginally

118 strained macrocyclic Möbius precursor in combination with [5]helicene as a

119 hidden writhe, and sequential aromatization of the cyclohexadiene units in

120 macrocyclic Möbius precursor would readily build up strained Möbius

121 conjugated all-carbon nanohoop.[26] More importantly, the presence of

122 [5]helicene subunit in Möbius conjugated carbon nanohoops eventually provide

123 the cyclic conjugation paths with 4n π-electrons (Figure 1 B), that is, **[5]H-**

124 **[7]CPP** contains 44 and 36 π electrons in the peripheric and inner conjugation

125 circuits, respectively; for **[5]H-[8]CPP**, those are 48 and 40 ones, respectively,

126 which are ready for investigating the relationship between [4n]Möbius topology

127 and aromaticity in present work.

128   The synthetic routes to **[5]H-[7]CPP** and **[5]H-[8]CPP** are outlined in

129 Scheme 1. The targeted Möbius nanohoop **[5]H-[7]CPP** was synthesized by

130 Suzuki-Miyaura cross-coupling between dibromopentahelicene **1** [41] and C-

131 shaped synthon **2** to give **3**, [42] followed by a reductive aromatization in 12%

132 yield over two steps. In the case of **[5]H-[8]CPP,** compound **4** was generated

133 in a yield of 80% by Suzuki coupling reaction between **1** and 4-

134 chlorophenylboronic acid, and was then converted to borate ester **5** in a yield

135 of 85%. Compound **7** was obtained by the Suzuki coupling reaction of **5** with L-

136 shaped synthon **6** in the presence of $Pd(PPh_3)_4$, 2M K_2CO_3 in deoxygenated

137 1,4-dioxane and H_2O in a yield of 72%. Precursor **8** was obtained by a ring-

138 closure reaction via a nickel-mediated Yamamoto reaction without further

139 purification, [43-44] subjected to a reductive aromatization using freshly made

140 H_2SnCl_4 in anhydrous THF at room temperature to afford the final nanohoop

141 **[5]H-[8]CPP** as a yellow solid in a total yield of 35%. The chemical structures

142 of **[5]H-[7]CPP** and **[5]H-[8]CPP** were confirmed by NMR, X-ray

143 crystallography and high-resolution mass spectra (see the Supporting

144 Information).
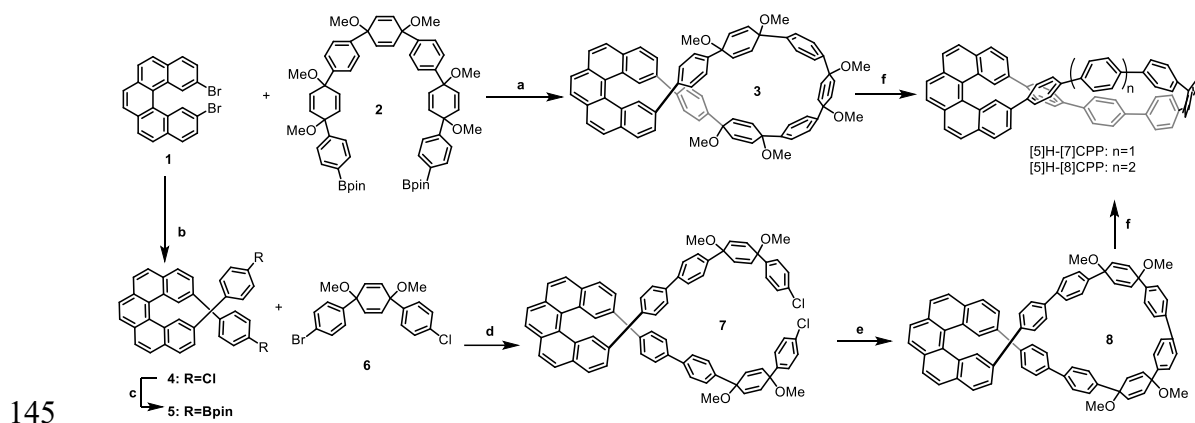
146 **Scheme 1.** Synthesis of **[5]H-[7, 8]CPP**. (a) 2M NaOH, Pd(PPh$_3$)$_4$, 1,4-dioxane, H$_2$O, 115 ℃, overnight,

147 without purification; (b) 4-Chlorophenyboronic acid, 2M Cs$_2$CO$_3$, Pd(PPh$_3$)$_4$, 1,4-dioxane, H$_2$O, 115 ℃,

148 overnight, 80%; (c) X-phos, Pd$_2$(dba)$_3$, B$_2$pin$_2$, KOAc, 1,4-dioxane, 115 ℃, overnight, 85%; (d) 2M K$_2$CO$_3$,

149 Pd(PPh$_3$)$_4$, 1,4-dioxane, H$_2$O, 115 ℃, overnight, 72%; (e) bpy, Ni(COD)$_2$, THF, 75 ℃, overnight, without

150 purification; (f) H$_2$SnCl$_4$, THF, RT, overnight, 12% for **[5]H-[7]CPP** and 35% for **[5]H-[8]CPP**.

151 **Structural analysis**

152 The single crystals of **[5]H-[7]CPP** were obtained by slowly volatilizing a

153 chloroform solution at 4 ℃, while the single crystals of **[5]H-[8]CPP** were

154 obtained by crystalizing its solution in a mixture of DCM/toluene (1:1, v/v) at the

155 same temperature. The single crystal X-ray analysis showed that **[5]H-[7]CPP**

156 was crystallized in triclinic *P1* space group, while**[5]H-[8]CPP** was solved in

157 orthorhombic *Pnna* space group. In each case, two pairs of enantiomers were

158 found in each unit cell. As shown in Figure 2, the crystal structures clearly

159 demonstrate that **[5]H-[7]CPP** and **[5]H-[8]CPP** possess a Möbius topology

160   with a reasonable conjugation. For **[5]H-[7]CPP**, the dihedral angles of the

161   adjacent six-membered rings as shown in Figure 2c are found to be from 26.4°

162   to 44.8°, while those for **[5]H-[8]CPP** are from 31.1° to 38.7° (Figure 2f) (Table

163   1). The fluctuated extent of the dihedral angles for **[5]H-[7]CPP** is larger than

164   those for **[5]H-[8]CPP,** mainly due to its larger strain in **[5]H-[7]CPP,** which is

165   supported by the DFT calculations (*vide infra*). The dihedral angles of **[5]H-**

166   **[7]CPP** and **[5]H-[8]CPP** in the solid phases are in good agreement with those

167   predicted   by   DFT   (b3lyp/6-31g(d)/PCM-UFF)   symmetry-unconstrained

168   calculations (in both the range and the average value) (Table 1 and Figure

169   S15b-S16b). The same arguments also hold for the torsional angles (Figure

170   S19-S20, Table S6-S7). In particular, in all the case of the crystal and the DFT-

171   optimized structures of **[5]H-[7, 8]CPP**, the lengths of the C_{ortho}–C_{ortho} bonds in

172   the *p*-phenylene units are pretty close to the neighbouring C_{ipso}–C_{ipso} ones

173   (Table   1),   implying   that   these   six-membered   rings   adopt   a   benzene-like

174   structure.

175   The strain energies of the Möbius nanohoops were estimated by DFT

176   calculations according to the homodesmotic reactions shown in Scheme S5,

177   wherein the nanohoops and biphenyl are converted to diphenyl[5]helicenes and

178   terphenyl. The strain energies of **[5]H-[7]CPP** and **[5]H-[8]CPP** are calculated

179   to be 52.5 and 47.8 kcal mol^{-1}, respectively, which indicates that **[5]H-[7]CPP**

180   is less stable due to the smaller size of the nanohoop as expected. Such strain

181 energies of **[5]H-[7]CPP** and **[5]H-[8]CPP** are close to those of [11]CPP (54

182 kcal mol^{-1}) and [12]CPP (48 kcal mol^{-1}), but are significantly smaller than those

183 of [7]CPP (84 kcal mol^{-1}) and [8]CPP (72 kcal mol^{-1}), [46] respectively, indicating

184 that the presence of [5]helicene moiety substantially decrease the tension of

185 [n]CPP nanohoops possessing the same number of paraphenylene units.

186 Moreover, it is worth noting that the strain energy of **[5]H-[7]CPP** is smaller than

187 that (55.4 kcal mol^{-1}) of Šolomek's [6]helicene nanohoop with the same

188 numbers of paraphenylene units, [26] suggesting that the [5]helicene nanohoops

189 might be more stable.

190
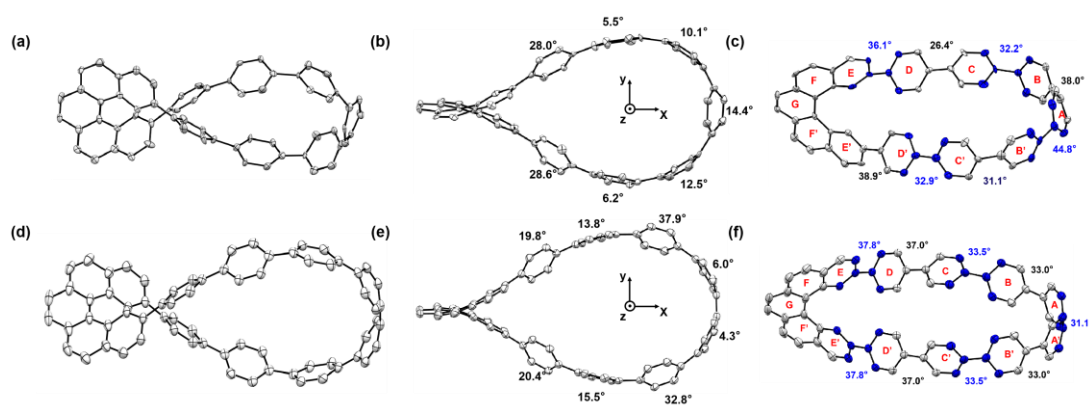
Figure 2. Single-crystal X-ray structures of (a–c) **[5]H-[7]CPP** and (d–f) **[5]H-[8]CPP**, with carbon atoms depicted using thermal ellipsoids set at the 50% probability level: the (a,d) side and the (b,e) top views. Only the *P*-enantiomers are shown for clarity. The intersection angles between the benzene rings and the *Z*-axis are provided in Figure 2b,e in degrees; and the related dihedral angles between the adjacent six-membered rings are shown in Figure 2c,f.

Table 1. C–C bond lengths (Bond length, [Å]), dihedral angles between benzene rings and the neighboring aryl rings (Dihedral angle, [°]), as well as the intersection angles between the benzene rings and the axis*a*

Parameters	**[5]H-[7]CPP** (crystal)	**[5]H-[7]CPP** (DFT-optimized)	**[5]H-[7]CPP²⁺** (DFT-optimized)	**[5]H-[8]CPP** (crystal)	**[5]H-[8]CPP** (DFT-optimized)	**[5]H-[8]CPP²⁺** (DFT-optimized)
Bond lengths [Å]: [c]						
C_{ortho}-C_{ortho}	1.372	1.391	1.377	1.385	1.391	1.379
C_{ipso}-C_{ortho}	1.389	1.408	1.421	1.394	1.407	1.420
C_{ipso}-C_{ipso}	1.499	1.487	1.457	1.487	1.486	1.460
Dihedral angle [°]: [d]	26.4–44.8 (35.1)	24.9–47.1 (36.8)	24.3–60.0 (40.0)	31.1–37.8 (34.9)	25.7–45.2 (35.3)	25.6–55.5 (38.0)
Intersection angle [°]: [d]	5.5–28.6 (15.0)	4.5–29.4 (15.3)	3.9–22.0 (9.0)	4.3–37.9 (18.8)	1.7–23.6 (14.0)	2.4–27.5 (9.9)

Optical properties

204   The photophysical properties of **[5]H-[7]CPP** and **[5]H-[8]CPP** were first

205   examined by UV−vis and fluorescence spectroscopies. The results are shown

206   in Figure 3 and the determined corresponding photophysical parameters are

207   summarized in Table 2. Basically, **[5]H-[7]CPP** in DCM displays the main

208   absorption peak at 338 nm with a molar extinction coeffecient (ε) of 8.2×10^4

209    $M^{-1}\ cm^{-1}$ and a shoulder band in the range of 370 − 450 nm, resembling that of

210   Šolomek's [6]helicene nanohoop. **[5]H-[8]CPP** shows a very similar absorption

211   contour, but with a larger ε of $9.8 \times 10^4\ M^{-1}\ cm^{-1}$ (Table 2).

212　　　　　The Möbius nanohoops show strong fluorescence in DCM with the

213　emission maximum at 492 nm and 482 nm for **[5]H-[7]CPP** and **[5]H-[8]CPP**,

214　respectively, which is red-shifted by 93 nm and 83 nm, respectively, compared

215　to that of [5]helicene (λ_{em}= 430 nm). When compared with [7]CPP, the

216　fluorescence maximum of **[5]H-[7]CPP** is blue-shifted by 97 nm. Similarly, the

217　peak of **[5]H-[8]CPP** is blue-shifted by 50 nm as compared to [8]CPP. These

218　are as expected due to the bigger size of these two molecules. The

219　fluorescence quantum yields (Φ_F) were determined to be 37.1% for **[5]H-**

220　**[7]CPP** and 44.6% for **[5]H-[8]CPP**, which are moderate but significantly higher

221　than those of the pristine [7-8]CPPs [47-48] and [5]helicene. [49-50] The symmetry

222　breaking caused by the presence of [5]helicene moiety in the nanohoops is

223　partially responsible for the turn-on fluorescence of [5]helicene-based

224　nanohoops. [52] The enhancement in fluorescence quantum yields were further

225　interpreted by theoretic calculations (*vide infra*). The fluorescence lifetimes (τ)

226　of **[5]H-[7]CPP** and **[5]H-[8]CPP** were determined to be 3.0 ns and 3.1 ns,

227　respectively, by single-exponential decay fitting (Figure S31-S32); and the

228　radiative decay rate constants (k_r) were corresponded to be 1.24×10^8 s^{-1} for

229　**[5]H-[7]CPP** and 1.44×10^8 s^{-1} for **[5]H-[8]CPP**, respectively. The Stokes shifts

230　are 154 nm and 144 nm for **[5]H-[7]CPP** and **[5]H-[8]CPP**, respectively. The

231　large Stokes shifts are mainly attributed to the significant structural relaxation

232　that occurs from the Franck-Condon state to the relaxed state.[51]
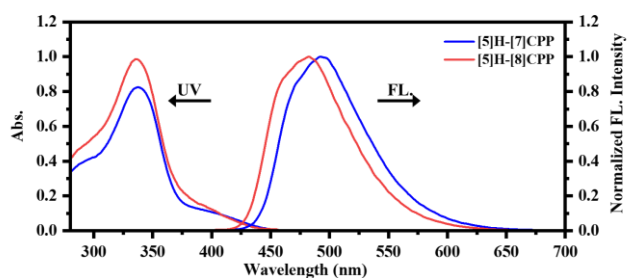
233

234 **Figure 3.** The UV-vis absorption and fluorescence emission spectra of **[5]H-[7]CPP** (blue) and **[5]H-**

235 **[8]CPP** (red) in CH_2Cl_2 (1.0×10^{-5} M).

236 **Table 2**. Photophysical properties of **[5]H-[7]CPP** [a], **[5]H-[8]CPP** [a], [7]CPP [47], [8]CPP [48] and [5]Helicene

237 [49-50].

Compd.	λ_{Abs} [b]/nm	$\varepsilon_m \times 10^4$	λ_{em} [c]/nm	Φ_F [d]/%	τ [e]/ns	Stokes Shift [f]/nm
[5]H-[7]CPP	338	8.2	492	37.1	3.0	154
[5]H-[8]CPP	338	9.8	482	44.6	3.1	144
[7]CPP [g]	340	6.9	587	0.7	NA	247
[8]CPP [g]	340	10.0	533	10	17.6	193
[5]Helicene [g]	305	10.0	400	4	25.5	95

238 [a] UV-vis absorption and fluorescence spectra were measured in DCM (1.0×10^{-5} M) at room temperature.

239 [b] Maximum absorption. [c] Maximum emission upon excitation at 338 nm. [d] Fluorescence quantum yields

240 in DCM solution were measured by using a calibrated integrating sphere system within ±3% error, excited

241 at 338 nm. [e] Lifetimes were measured in DCM (1.0×10^{-5} M, λ_{ex}=338 nm). [f] Stokes shift was calculated

242 based on λ_{em}-λ_{Abs}. [g] Compounds [7-8]CPPs and [5]Helicene were synthesized according to the reported

243 procedures (ref. 47-50) and their photophysical properties were measured under identical conditions.

244 The frontier molecular orbitals (FMOs) calculated at MN15/6-31g* level

245 reveal similar orbital characteristics for **[5]H-[7]CPP** and **[5]H-[8]CPP** (Figure 4

246 and S42-S44). Both HOMO and LUMO mainly concentrate on the

paraphenylene moieties, whereas HOMO-1 and LUMO+1 are comparatively

more dispersed and mainly scattered over the [5]helicene subunits. The energy

diagrams of the dominant excitations are shown in the left of Figure 4. In both

cases, the absorption bands at 338 nm are mainly attributed to transitions from

HOMO-1→LUMO and HOMO→LUMO+1, which are corresponding to the

calculated absorption maxima at 330 nm for **[5]H-[7]CPP** and 333 nm for **[5]H-**

[8]CPP, respectively, with the large oscillator strength (f) values. The small

shoulder bands around 400 nm are corresponding to the transition of

HOMO→LUMO. Note that the FMOs of [5]helicene are no longer HOMOs and

LUMOs of **[5]H-[7]CPP** and **[5]H-[8]CPP** so that the emission wavelength are

mainly dependent on the cyclic paraphenylene units, which are presumably

accountable for the fact that the fluorescence quantum yields of [5]helicene-

based nanohoops are significantly higher than that of the pristine [5]helicene.

[5]H-[7]CPP features the HOMO and the LUMO energy level of -5.21 and -1.74

eV, respectively, slightly wider than that of **[5]H-[8]CPP** corresponding to -5.20

and -1.78 eV, respectively (Figure 4). The HOMO−LUMO gaps of **[5]H-[7]CPP**

and **[5]H-[8]CPP** are determined to be 3.47 and 3.42 eV, respectively, which

are slightly narrower than those of [11]CPP and [12]CPP (3.49 and 3.56 eV,

respectively). **[5]H-[7]CPP** exhibits a notably larger HOMO-LUMO gap than

7CPP (3.15 eV), while **[5]H-[8]CPP** possesses a slightly larger HOMO-LUMO

gap, compared to 8CPP (3.36 eV, MN15/6-31g* level). [53]
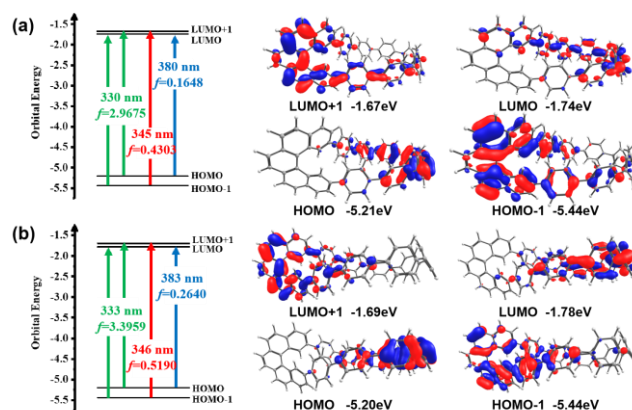
Figure 4. Energy diagrams and pictorial representations of the FMOs for (a) **[5]H-[7]CPP** and (b) **[5]H-[8]CPP**. The values of *f* represent the oscillator strengths.

Chiral resolutions of the enantiomers of **[5]H-[7]CPP** and **[5]H-[8]CPP** were achieved by HPLC with a chiral-stationary-phase column (Chiralpak IB column, 4.6 mm Φ × 250 mm L) and a UV detector, using DCM/*n*-heptane (40:60) as the mobile phase with a flow of 2 mL/min. Each pair of enantiomers were obtained as a pair of isolated fractions with a ratio of about 1:1, respectively (Figure S36). The ECD spectra of the two isolated HPLC fractions recorded in DCM solution (Figure 5a and 5b) were perfect mirror images corresponding to the *P*- and *M*-enantiomers of **[5]H-[7]CPP** and **[5]H-[8]CPP**, respectively, which were assigned according to the computational studies (Figure S47). The ECD spectra of enantiomers display multiple Cotton effects in the range of 235 to 435 nm, with two distinct sign inversions at λ = 310 and 374 nm for **[5]H-[7]CPP** and at λ = 314 and 374 nm for **[5]H-[8]CPP** (Figure 5

284   and S37), respectively. The enantiomers of **[5]H-[7]CPP** exhibits a maximum

285   CD signal at 350 nm with $|\Delta\varepsilon|$ = 61.8 M^{-1} cm^{-1} and the $|g_{abs}|$ value of 2.7×10^{-3},

286   while the enantiomers of **[5]H-[8]CPP** also exhibits a maximum CD signal at

287   the same wavelength but with a larger $|\Delta\varepsilon|$ = 88.5 $M^{-1}cm^{-1}$ and $|g_{abs}|$ = 3.3×10^{-3}

288   (Figure S38).

289   The chiroptical properties of the excited states were investigated by the

290   means of circularly polarized luminescence (CPL) spectroscopy. The two

291   enantiomers of **[5]H-[7]CPP** and **[5]H-[8]CPP** show CPL emission in the range

292   of 430 to 700 nm (Figure 5), which are corresponding to the fluorescence

293   emission. The CPL spectra of each pair of enantiomers are mirror images of

294   each other. The maximum CPL dissymmetry factor ($|g_{lum}|$) can evaluate the

295   magnitudes of CPL, thus the $|g_{lum}|$ values were determined to be 1.40 $\times10^{-3}$ and

296   1.26 $\times10^{-3}$ for **[5]H-[7]CPP** and **[5]H-[8]CPP**, respectively, which are in the

297   range of 10^{-5} to 10^{-3} for small organic molecules. [54-58] The ratios of $|g_{lum}|$ and

298    $|g_{abs}|$ were calculated to be 0.52 and 0.38 for **[5]H-[7]CPP** and **[5]H-[8]CPP**,

299   respectively. The values are likely to indicate that the geometric change

300   between the ground and excited states is relatively small for **[5]H-[7]CPP** but

301   significant for **[5]H-[8]CPP,** which is presumably due to that the structure in

302   excited state of **[5]H-[7]CPP** is more rigid than that of **[5]H-[8]CPP**. [54-61]

303
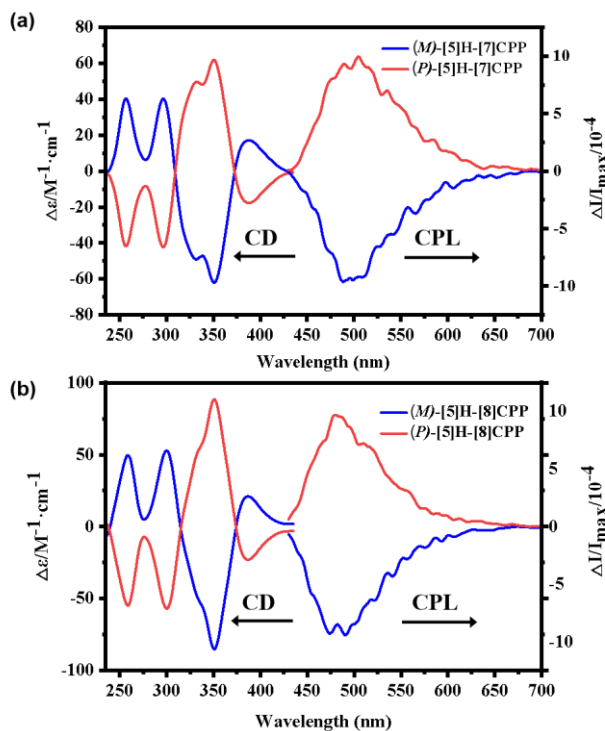
Figure 5. CD and CPL spectra of (a) **[5]H-[7]CPP** and (b) **[5]H-[8]CPP** in DCM ($1.0{\times}10^{-5}$M).

305

Electronic Structures of the Neutral Species

307   To understand the electronic structures of the neutral compound and its

308   aromaticity, Nucleus-independent chemical shifts (NICS) analysis was first

309   carried out. The NICS($\pm$1)$_{zz}$ values of all the six-membered rings of the studied

310   neutral systems, obtained from the GIAO-B3LYP/6-31g(d,p) computations, are

311   largely negative (Figure S48, Table S19), indicative of a strong aromaticity of

312   these moieties. Geometric aromaticity analyses, on the basis of the structures

313   optimized at the B3LYP/6-31g(d) level, provided accordant results. In both of

314   **[5]H-[7]CPP** and **[5]H-8]CPP**, the harmonic oscillator model of aromaticity

315 (HOMA) values are determined to be 0.989-0.993 of the *p*-phenylene units,

316 revealing that these rings are highly aromatic. Values of about 0.950 of the

317 peripheral rings and 0.84-0.89 for the rest ones in the [5]helicene moiety are

318 obtained, which is due to the twisted conformation and the strong π-conjugation

319 in this unit (Figure S26-S27, Table S11 and S12).

320 Interestingly, the calculated $NICS_{zz}$ values show some differences on the

321 periphery and interior cavity of the Möbius nanohoops (Figure S48-S49). For

322 the ghost atoms located at the periphery of the nanohoop for a specific ring, the

323 value is typically less negative compared to the corresponding one located

324 inside, suggestive of a more aromatic circumstance for the inner cavity of the

325 nanohoops [62]. Further NICS-scan was carried out, in which the NICS probes

326 were placed the inner cavity of the nanohoops at intervals of 2.61 and 2.91 Å

327 to give a quinque-section in the case of **[5]H-[7]CPP** and **[5]H-[8]CPP**,

328 respectively, along the theoretical C_2 axis of symmetry.

329 As shown in Figure 6, ignoring place A that located in the bay area of the

330 [5]helicene moiety, the NICS values at the inner cavity are in the range from -

331 7.2 to -5.3 and from -9.8 to -4.0 ppm for **[5]H-[7]CPP** and **[5]H-[8]CPP**,

332 respectively. These small negative NICS values could be due to the presence

333 of marginal aromaticity and the small positive values of position A might be

334 ascribed to the, comparatively, stronger paratropic current flowing in the bay of

335 the helicene moiety. Therefore, NICS-scan analyses are suggestive of local

336　　Hückel aromaticity for the neutral species of the studied molecules. Such a local

337　　aromaticity is supported further by the two-dimensional nucleus-independent

338　　chemical shift value (2D-NICS) calculations (Figure 8c and S54 and S56),

339　　which show that no obvious shielding can be observed in the inner cavity of the

340　　hoops.

Species	A	B	C	D	E
[5]H-[7]CPP	2.60	-7.20	-6.45	-5.33	-6.24
[5]H-[7]CPP^{2+}	-27.2	-71.3	-77.9	-78.5	-97.0
[5]H-[8]CPP	4.20	-9.77	-5.34	-4.76	-4.00
[5]H-[8]CPP^{2+}	-17.5	-43.8	-42.7	-42.7	-53.9
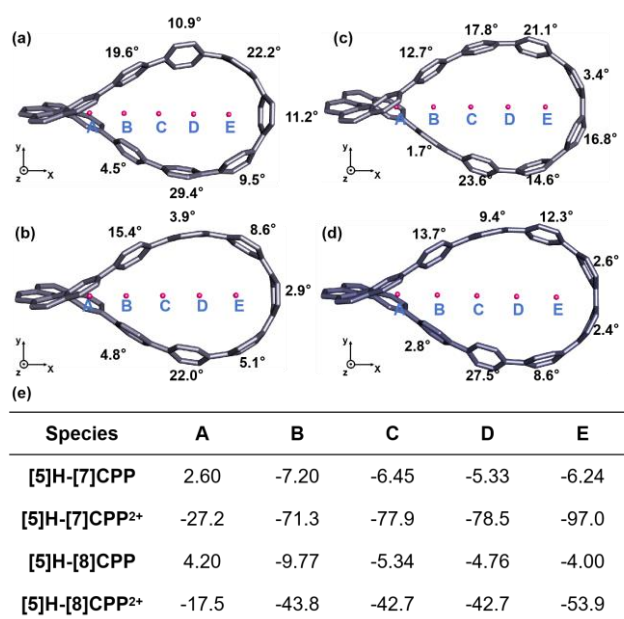
341

342　**Figure 6.** NICS(0)$_{zz}$ values calculated at GIAO-B3LYP/6-31g(d,p) level of theory at points of quinque-
343　section (ghost atom A to E) of the inner cavities of (a) **[5]H-[7]CPP** and (b) **[5]H-[7]CPP^{2+}**, (c) **[5]H-[8]CPP**
344　and (d) **[5]H-[8]CPP^{2+}** along the theoretical C_2 axis of symmetry. The values are shown in the table (Figure
345　6e) below the DFT-optimized structures. The external magnetic field is oriented along the z axis. The
346　black numbers shown in the Figures (a-d) correspond to the intersection angles (in degrees) between the
347　benzene rings and the Z-axis.

348　　　　Anisotropy of the induced current density (AICD) analyses are widely

349　　accepted for visualization of aromaticity. [3, 22-25, 53-67] The AICD plot (isovalue =

350　　0.040) of **[5]H-[7]CPP** clearly shows locally diatropic currents in each individual

351　　benzene ring (Figure 8a,b). For the [5]helicene moiety, a strong diatropic

352　　current can be observed in the periphery and a paratropic current presents in

353   the bay. Similar pattern is also observable in the case of **[5]H-[8]CPP** (Figure

354   S60). Such AICD plots is strongly indicative of a local aromaticity for both **[5]H-**

355   **[7]CPP** and **[5]H-[8]CPP**.

356   The isolated electron density observed in the localized orbital locator-π

357   (LOL-π) plots [68-69] are in good agreement with the results of the NICS and AICD

358   analysis as well. In the case of **[5]H-[7]CPP**, at isovalue = 0.30 level, the π-

359   electrons delocalize over all the [5]helicene moiety and the individual benzene

360   rings (Figure 7a). Nevertheless, the π-electrons do not spread continuously in

361   the whole [7]cycloparaphenylenes fragment, and bifurcations located at the

362   bridging C–C single bonds are observed, indicating that the π-conjugation

363   within **[5]H-[7]CPP** is not significant enough, inhibiting the system to display

364   global aromaticity. For **[5]H-[8]CPP**, a similar, but less continuous, π-electrons

365   delocalization pattern is shown, suggestive of a weaker electron conjugation

366   (Figure 7e). This phenomenon, similar to those of their parent molecules

367   [n]CPPs, [47, 48, 52] is understandable because that a smaller nanohoop would give

368   rise to a better radial π-overlap and thus an effective increase in the π-

369   conjugation between the neighbouring aryl rings. Notably, LOL-σ plots at

370   isovalue = 0.60 clearly show that the electrons delocalization on the C–C atoms

371   bridged neighbouring aryls are comparable to that over the benzene rings

372   (Figure 7, b and f), suggesting that **[5]H-[7]CPP** and **[5]H-[8]CPP** are still

373   conjugated to some extent.
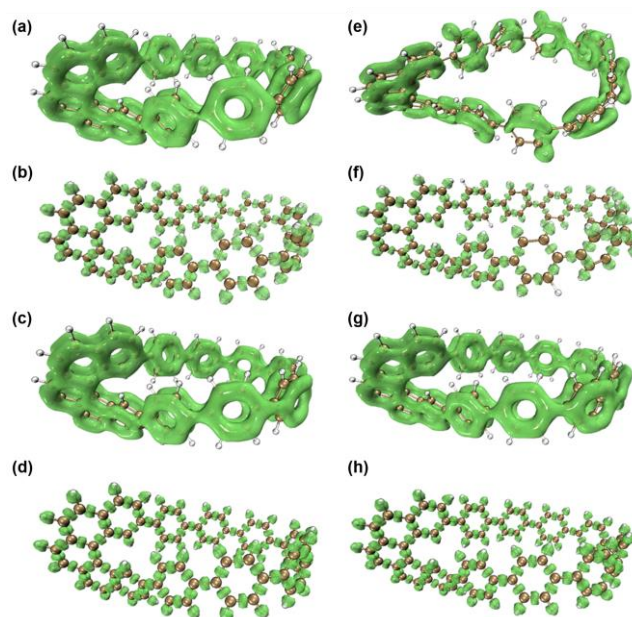
Figure 7. (a,c,e,g) LOL-π (isovalue = 0.30) and (b,d,f,h) LOL-σ (isovalue = 0.60) isosurfaces for (a,b)

[5]H-[7]CPP, (c,d) **[5]H-[7]CPP^{2+}**, (e,f) **[5]H-[8]CPP** and (g,h) **[5]H-[8]CPP^{2+}**

Electronic Structures of the Dications

We expected that the dications of the studied nanohoops, **[5]H-[7,8]CPP^{2+}**,

may possess different aromatic characters compared to their neutral analogues.

Theoretically, the dications of **[5]H-[7,8]CPP** have cyclic conjugation paths with

4n+2 π-electrons in both the peripheric and inner conjugation circuits, which

match the π-electron rule of either Möbius anti-aromaticity or Hückel aromaticity.

We next tried to prepare the dicationic **[5]H-[7,8]CPP**. Cyclic voltammetry (CV)

of **[5]H-[7]CPP** in 0.1 M tetrabutylammonium hexafluorophosphate ([n-

Bu$_4$N]$^{+}$[PF$_6$]$^{-}$) in DCM showed a wave, not fully reversible, at E$_{ox}$ = +0.385 V vs

Fc/Fc^{+} (Figure S41). Accordingly, tris(4-bromophenyl) ammoniumyl

hexachloroantimonate (Magic Blue, +0.7 V vs Fc/Fc^{+}) [70] was chosen to oxide

388   **[5]H-[7]CPP** in DCM at room temperature. Unexpectedly, a white diamagnetic

389   product with complicated ^{1}H NMR signals was isolated (Figure S2-S3 and S6).

390   An attempt to crystalize the white product was unsuccessful. However, a mass

391   peak of *m/z* = 1615.6131 was detected by the MOLDI-TOF-HRMS spectrum

392   (Figure S4), which is presumably assignable to a dimer of **[5]H-[7]CPP**

393   (Scheme S2), according to the observations reported by Kayahara, *et al.*[27]

394   However, we preferred not to incur further discussion on the detailed structural

395   assignment.

396   The unsuccessful synthesis of the dications compelled us to solely explore

397   the electronic structures computationally. Like **[5]H-[7]CPP**, the DFT (b3lyp/6-

398   31g(d) optimized structure of **[5]H-[7]CPP^{2+}** show a Möbius topology as well

399   (Figure 6a–d). Nevertheless, compared to the neutral species in which the *p*-

400   phenylene units are somewhat staggered, the *p*-phenylenes in **[5]H-[7]CPP^{2+}**

401   are more parallel to the axle of the hoop along which the 2D projection exhibits

402   the largest macrocyclic area (i.e., the *Z*-axis shown in Figure 6) (with the

403   intersection angles of 2.9–22.0°, compared to 5.5–28.6 for **[5]H-[7]CPP**) (Table

404   1, Figure 2b,e and Figure 6), so that their *p* orbitals are more radially oriented,

405   implied of a higher π-conjugation of the whole systems. In regard to the bond

406   lengths, though there are no obvious changes for those in the [5]helicene

407   subunit (Table S9), the C_{ortho}–C_{ortho} and C_{ipso}–C_{ipso} bonds in the *p*-phenylene

408   units contract to some extent (1.377 and 1.457 Å, respectively, in average,

409   compared to 1.391 and 1.487 Å, respectively, for **[5]H-[7]CPP**), whereas the

410   C_{ipso}–C_{ortho} bond elongate slightly (1.421 vs 1.408 Å, averagely, for **[5]H-**

411   **[7]CPP**)[31] (Table 1), which is indicative of an increase in the quinoidal

412   contribution to the cycloparaphenylenes moiety. Notably, the HOMA values

413   (0.989-0.993) for the *p*-phenylene rings in **[5]H-[7]CPP^{2+}** are very close to those

414   (0.989-0.992) in **[5]H-[7]CPP** (Table S11 and Figure S26). This indicates that

415   HOMA is not a good parameter to evaluate the aromaticity character in our

416   cases in which the changes of length show different trends for different bonds.

417   Very similar results are also obtained for **[5]H-[8]CPP^{2+}**. (Table 1 and S12,

418   Figure S27).

419   The strain energies of the dicationic nanohoops were estimated based on

420   the homodesmotic reactions associating conversions from the dicationic

421   nanohoops and biphenyl to diphenyl[5]helicene radical cation as well as the

422   radical-cationic and the neutral terphenyls (Scheme S6), which gave a value of

423   41.2 and 36.8 kcal mol^{-1} for **[5]H-[7]CPP^{2+}** and **[5]H-[8]CPP^{2+}**, respectively, ca.

424   11 kcal mol^{-1} smaller than that of the neutral one in both the cases. The lower

425   strain energies represent that the quinoidal contribution is helpful to stabilize

426   the Möbius topology.

427   The NICS($\pm$1)$_{zz}$ values of the *p*-phenylene rings in **[5]H-[7,8]CPP^{2+}** are still

428   largely negative, but less as compared to those of the neutral species (Figure

429   S48-S49), indicative of a decrease in the local aromaticity for the benzene rings

430 in the dications adopting a quinoid-like structure. In contrast, for the six-

431 membered rings in [5]helicene units, the values become much more negative.

432 In particular, extremely negative values (for example, less than –130 ppm in the

433 case of **[5]H-[7]CPP^{2+}**) are observed for the two rings adjacent to the central

434 six-membered rings, suggesting the presence of strong local diatropic ring

435 current in an external magnetic field. NICS-scanning in which the probes were

436 placed in quinque-section points of the inner cavity along the C_2 axis gave rise

437 to very negative values in both the case of **[5]H-[7]CPP^{2+}** and **[5]H-[8]CPP^{2+}**

438 (Figure 6, Figure S51 and S53). This strongly indicates that, distinct from their

439 neutral analogues, **[5]H-[7,8]CPP^{2+}** possess a global aromaticity character.

440 Further, the global aromaticity of such aromatic systems is provided by 2D-

441 NICS calculations. As shown in Figure 8f and Figure S55 and S57, consistent

442 with the corresponding computed NICS$_{zz}$ values, a very strong shielding effect

443 caused by the diatropic ring current on the nanohoops is observed on their inner

444 cavities due to the formation of in-plane aromaticity, which is in sharp contrast

445 with that in the cases of the neutral species (Figure 8c and S54 and S56).

446 AICD analyses provide more details of the global aromaticity. In both the

447 case of **[5]H-[7,8]CPP^{2+}** (Figure S59 and S61), the AICD plot shows a

448 continuous, strong counter-clockwise paratropic ring current along the whole

449 molecular periphery (Figure 8e and figure S61b). More careful observation

450 reveals that, under the perspective of a front view (Figure 8d and figure S61a),

451   the induced electron flow is significant along, first, the lower rim of the

452   cycloparaphenylenes fragment and, then, the periphery of the [5]helicene unit,

453   followed the upper rim of the cycloparaphenylenes fragment on the back. By

454   this way, the current-flow lifts the restriction of Möbius topology to exhibit in-

455   plane global aromaticity, resembling that of the dications of [n]CPPs. Local

456   vortices of current are observable on the two six-membered rings adjacent to

457   the central ring of the [5]helicene unit, which is indicative of a non-negligible

458   local aromaticity contribution, in agreement with the corresponding highly

459   negative $NICS(\pm1)_{zz}$ values of these two rings.

460   The LOL-π plots (isovalue = 0.30) (Figure 7) show that, compared to **[5]H-**

461   **[7,8]CPP**, the π-electrons on **[5]H-[7,8]CPP²⁺** are more thoroughly distributed

462   throughout the [5]helicene moiety and the whole [7]cycloparaphenylenes

463   fragment to form a big conjugated structures, which is in coincidence with the

464   character of global aromaticity of the systems. In contrast, the LOL-σ plots at

465   isovalue = 0.60 level of **[5]H-[7,8]CPP²⁺** display an almost identical pattern to

466   that of the neutral species, indicating that the σ aromaticity is similar before and

467   after the cationization.

468
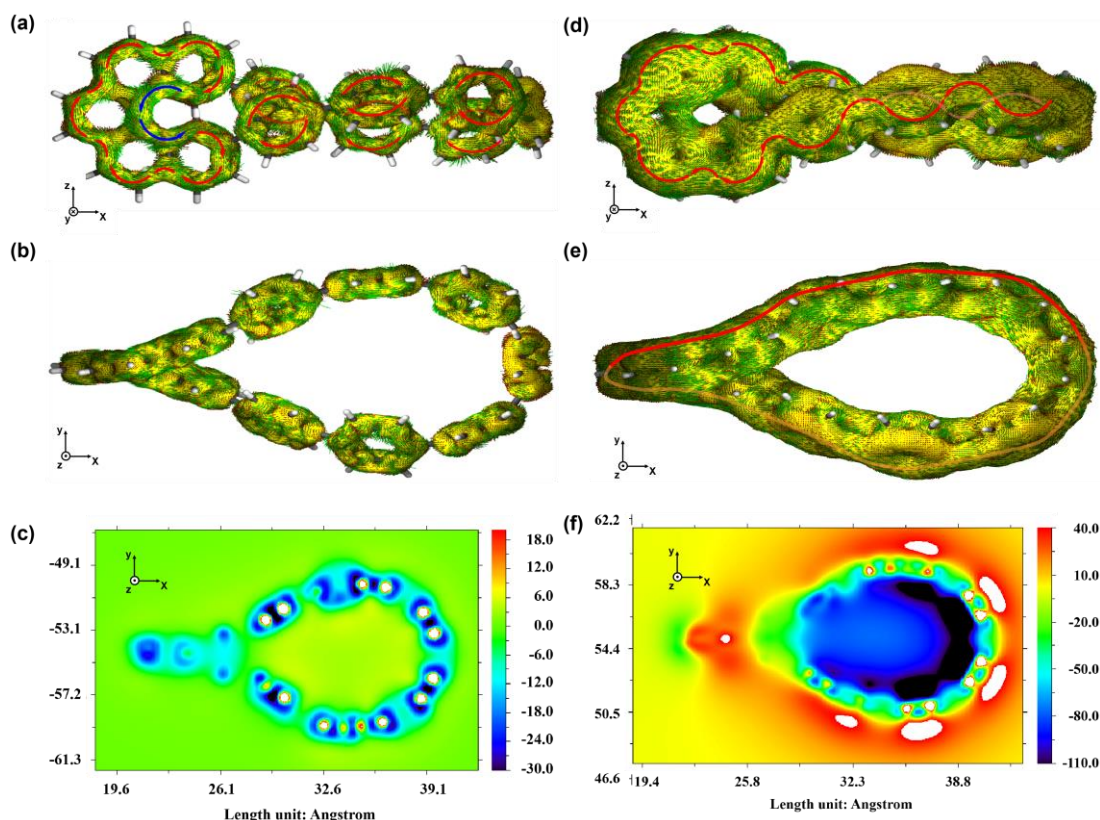
Figure 8. The (a,d) front and (b,e) the top views of the AICD plots (isovalue = 0.040) as well as (c,f) the

2D-NICS grids calculated by the GIAO-B3LYP/6-31g(d,p) method for (a–c) **[5]H-[7]CPP** and (d–f) **[5]H-**

[7]CPP^{2+}. The diamagnetic (clockwise) and paramagnetic (counterclockwise) ring currents under the

magnetic field are highlighted by red and blue arrows, respectively. In all the cases, the external magnetic

field is oriented along the *Z*-axis.

Conclusions

In this study, two π-conjugated all-carbon nanohoops with a Möbius

topology by incorporating [5]helicene into oligoparaphenylene units are

prepared. X-ray structural analyses confirmed that the conjugated all-carbon

nanohoops exhibit a distinct Möbius topology. The photophysical and chiroptical

properties of the nanohoops were investigated after HPLC resolutions. The

chiral nanohoops display strong electronic circular dichroism signal with multi-bands in the spectra and bright CPL emissions, with moderately high absorption and luminescence dissymmetry factors. Theoretical structural analysis revealed that the presence of [5]helicene unit leads to a significant mitigation of strain and the cyclic conjugated pathways with 4n π-electrons. Though possessing a Möbius topology, our computational investigations revealed a weakly conjugated, locally Hückel-aromatic character of these all-carbon nanohoops in the neutral state, while their dicationic species exhibit in-plane global aromaticity, resembling that of [n]CPPs. The results may provide a better understanding of the complicated relationship between Möbius topology and aromaticity.

AUTHOR INFORMATION

Corresponding Author

Hua Jiang, College of Chemistry, Beijing Normal University, Beijing 100875 (P. R. China) Email: jiangh@bnu.edu.cn

Ying Wang, College of Chemistry, Beijing Normal University, Beijing 100875 (P. R. China) Email: ywang1@bnu.edu

503

504

REFERENCES

506 1 P. J. Garratt, *Aromaticity,* Wiley, **1986**, pp. 1-19.

507 2 T. M. Krygowsk, M. K. Cyrański, *Chem. Rev.* 2001, **101**, 1385-1419.

508 3 R. Herges, *Chem. Rev.* 2006, **106**, 4820-4842.

509 4 H. S. Rzepa, *Chem. Rev.* 2005, **105**, 3697-3715.

510 5 G. R. Schaller, R. Herges, *Chem. Commun.* 2013, **49**, 1254.

511 6 E. Heilbronner, *Tetrahedron Lett.* 1964, **5**, 1923–1928.

512 7 D. Ajami, O. Oeckler, A. Simon, R. Herges, *Nature.* 2003, **426**, 819-821.

513 8 M. Stępień, L. Latos-Graźyński, N. Sprutta, P. Chwalisz, L. Szterenberg,

514   *Angew. Chem. Int. Ed*. 2007, **46**, 7869-7873.

515 9 M. Stępień, N. Sprutta, L. Latos-Graźyński, *Angew. Chem. Int. Ed.* 2011,

516   **50**, 4288-4340.

517 10 S. Saito, A. Osuka, *Angew. Chem. Int. Ed.* 2011, **50**, 4342-4373;

518 11 Z. S. Yoon, A. Osuka, D. Kim, *Nat. Chem.* 2009, **1**, 113-122.

519   12 Y. Segawa, M. Kuwayama, Y. Hijikata, M. Fushimi, T. Nishihara, J.

520   Pirillo, J. Shirasaki, N. Kubota, K. Itami, *Science.* 2019, **365**, 272–276.

521   13 J. M. V. Raden, B. M. White, L. N. Zakharov, R. Jasti, *Angew. Chem.*

522   *Int. Ed.* 2019, **58**, 7341 –7345.

523   14 Y. Segawa, D. R. Levine, K. Itami, *Acc. Chem. Res.* 2019, **52**,

524   2760−2767.

525   15 Y. Segawa, M. Kuwayama, K. Itami, *Org. Lett.* 2020, **22**, 1067−1070.

526   16 J. M. V. Raden, N. N. Jarenwattananon, L. N. Zakharov, R. Jasti, *Chem.*

527   *Eur. J.* 2020, **26**, 10205–1020.

528   17 T. Muramats, Y. Okado, H. Traeger, S. Schrettl, N. Tamaoki, C. Weder,

529   Y. Sagara, *J. Am. Chem. Soc.* 2021, **143**, 9884−9892.

530   18 X. Zhang, H. Shi, G. Zhuang, S. Wang, J. Wang, S. Yang, X. Shao, P.

531   Du, *Angew. Chem. Int. Ed.* 2021, **60**, 17368 –17372;

532   19 X. Zhang, H. Liu, G. Zhuang, S. Yang, P. Du, *Nat. Commun.* 2022, **13**,

533   3543;

534   20 A. Bu, Y. Zhao, H. Xiao, C.-H. Tung, L.-Z. Wu, H. Cong, *Angew. Chem.*

535   *Int. Ed.* 2022, **61**, e202209449.

536   21 J. H. May, J. M. V. Raden, R. L. Maust, L. N. Zakharov, R. Jasti, *Nat.*

537   *Chem.* 2023, **15**, 170–176.

538   22 G. R. Schaller, F. Topić, K. Rissanen, Y. Okamoto, J. Shen, R. Herges,

539   *Nat. Chem.* 2014, **6**, 608-613.

540 23 G. Naulet, L. Sturm, A. Robert, P. Dechambenoit, F. Röhricht, R. Herges,

541   H. Bock, F. Durola, *Chem. Sci.* 2018, **9**, 8930−8936.

542 24 X. Jiang, J. D. Laffoon, D. Chen, S. Pérez-Estrada, A. S. Danis, J.

543   Rodríguez-López, M. A. Garcia-Garibay, J. Zhu, J. S. Moore, *J. Am.*

544   *Chem. Soc.* 2020, **142**, 6493-6498.

545 25 Y.-Y. Fan, D. Chen, Z.-A. Huang, J. Zhu, C.-H. Tung, L.-Z. Wu, H. Cong,

546   *Nat. Commun.* 2018, **9**, 3037.

547 26 J. Malinčík, S. Gaikwad, J. P. Mora-Fuentes, M. Boillat, A. Prescimone,

548   D. Häussinger, A. G. Campaña, T. Šolomek, *Angew. Chem. Int. Ed.* 2022,

549   **61**, e202208591.

550 27 T. Terabayashi, E. Kayahara, Y. Zhang, Y. Mizuhata, N. Tokitoh, T.

551   Nishinaga, T. Kato, S.Yamago, *Angew. Chem. Int. Ed.* 2023, **62**,

552   e202214960.

553 28 S. Nishigaki, Y. Shibata, A. Nakajima, H. Okajima, Y. Masumoto, T.

554   Osawa, A. Muranaka, H. Sugiyama, A. Horikawa, H. Uekusa, H. Koshino,

555   M. Uchiyama, A. Sakamoto, K. Tanaka, *J. Am. Chem. Soc.* 2019, **141**,

556   14955-14960.

557 29 S. Wang, J. Yuan, J. Xie, Z. Lu, L. Jiang, Y. Mu, Y. Huo, Y. Tsuchido,

558   K. Zhu, *Angew. Chem. Int. Ed.* 2021, **60**, 18443-18447.

559 30 Y. Segawa, T. Watanabe, K. Yamanoue, M. Kuwayama, K. Watanabe,

560   J. Pirillo, Y. Hijikata, K. Itami, *Nat. Synth.* 2022, **1**, 535-541.

561   31 B. Yao, X. Liu, T. Guo, H. Sun, W. Wang, *Org. Chem. Front.*, 2022, **9**,

562   4171–4177.

563   32 W. Fan, T. M. Fukunaga, S. Wu, Y. Han, Q. Zhou, J. Wang, Z. Li, X.

564   Hou, H. Wei, Y. Ni, H. Isobe, J. Wu, *Nat. Synth.* 2023, **2**, 880-887.

565   33 S. Wu, Y. Han, Y. Ni, X. Hou, H. Wei, Z. Li, J. Wu, *Angew. Chem. Int.*

566   *Ed.* 2024, **63**, e202320144.

567   34 S. Guo, L. Liu, F. Su, H. Yang, G. Liu, Y. Fan, J. He, Z. Lian, X. Li, W.

568   Guo, X. Chen, H. Jiang, *JACS Au*. 2024, **4**, 402–410.

569   35 S. Z. Guo, L. Liu, X. N. Li, G. Q. Liu, Y. Q. Fan, J. He, Z. Lian, H. J.

570   Yang, X. B. Chen, H. Jiang, *Small*. 2024, 2308429.

571   36 Y. -Q.; Fan, S. Fan, L. Liu, S. Z. Guo, J. He, X. -N. Li, Z. Lian, W. J. Guo,

572   X. B. Chen, Y. Wang, H. Jiang, *Chem. Sci.* 2023, **14**, 11121-11130.

573   37 Y. Q. Fan, J. He, S. Z. Guo, H. Jiang, *ChemPlusChem.* 2023,

574   e202300536.

575   38 Y. Q. Fan, J. He, L. Liu, G. Q. Liu, S. Z. Guo, Z. Lian, X. N. Li, W. J. Guo,

576   X. B. Chen, Y. Wang, H. Jiang, *Angew. Chem. Int. Ed.* 2023, **62**,

577   e202304623.

578   39 J. He, M. Yu, Z. Lian, Y. -Q. Fan, S. Z. Guo, X. -N. Li, Y. Wang, W. G.

579   Wang, Z. -Y. Cheng, H. Jiang, *Chem. Sci.* 2023, **14**, 4426-4433.

580   40 R. Jasti, J. Bhattacharjee, J. B. Neaton, C. R. Bertozzi, *J. Am. Chem.*

581   *Soc.* 2008, **130**, 17646-17647.

582 41 S. Jhulki, A. K. Mishra, T. J. Chow, J. N. Moorthy, *Chem. Eur. J.* 2016,

583   **22**, 9375-9386.

584 42 S. Wang, X. Li, X. Zhang, P. Huang, P. Fang, J. Wang, S. Yang, K. Wu,

585   P. Du, *Chem. Sci.* 2021, **12**, 10506-10513.

586 43 T. Yamamoto, T. Maruyama, Z.-H. Zhou, T. Ito, T. Fukuda, Y. Yoneda,

587   F. Begum, T. Ikeda, S. Sasaki, H. Takezoe, A. Fukuda, K. Kubota, *J. Am.*

588   *Chem. Soc.* 1994, **116**, 4832.

589 44 T. Yamamoto, K. Anzai, H. Fukumoto, *Chem. Lett.* 2002, **8**, 774-775.

590 45 J. K. Park, Z. S. Yoon, M.-C. Yoon, K. S. Kim, S. Mori, J.-Y. Shin, A.

591   Osuka, D. Kim, *J. Am. Chem. Soc.* 2008, **130**, 1824-1825.

592 46 Y. Segawa, H. Omachi, K. Itami, *Org. Lett.* 2010, **12**, 10, 2262–2265.

593 47 Y. Segawa, A. Fukazawa, S. Matsuura, H. Omachi, S. Yamaguchi, S.

594   Irle, K. Itami, *Org. Biomol. Chem.* 2012, **10**, 5979 and references therein.

595 48 E. R. Darzia, R. Jasti, *Chem. Soc. Rev.*, 2015, **44**, 6401-6410.

596 49 H. Kubo, T. Hirose, K. Matsuda, *Org. Lett.* 2017, **19**, 1776−1779.

597 50 J. B. Birks, D. J. S. Birch, E. Cordemans, E. V. Donckt, *Chem. Phys.*

598   *Lett.* 1976, **43**, 33−36.

599 51 C. Camacho, T. A. Niehaus, K. Itami, S. Irle, *Chem. Sci.*, 2013, **4**, 187–

600   195.

601 52 T. C. Lovell, C. E. Colwell, L. N. Zakharovb, R. Jasti, *Chem. Sci.* 2019,

602   **10**, 3786.

603 53 T. Iwamoto, Y. Watanabe, Y. Sakamoto, T. Suzuki, S. Yamago, *J. Am.*

604   *Chem. Soc.* 2011, **133**, 21, 8354-8361.

605 54 E. M. Sánchez-Carnerero, A. R. Agarrabeitia, F. Moreno, B. L. Maroto,

606   G. Muller, M. J. Ortiz, S. D. l. Moya, *Chem. Eur. J.* 2015, **21**, 13488–

607   13500.

608 55 D. Zheng, L. Zheng, C. Yu, Y. Zhan, Y. Wang, H. Jiang, *Org. Lett.* 2019,

609   **21**, 2555–2559.

610 56 D. Zheng, C. Yu, L. Zheng, Y. Zhan, H. Jiang, *Chin. Chem. Lett.* 2020,

611   **31**, 673–676.

612 57 D. Zheng, S. Guo, L. Zheng, Q. Xu, Y. Wang, H. Jiang, *Chem. Commun.*,

613   2021, **57**, 12016.

614 58 J. He, M. Yu, M. Pang, Y. Fan, Z. Lian, Y. Wang, W. Wang, Y. Liu, H.

615   Jiang, *Chem. Eur. J.* 2022, **28**, e202103832.

616 59 Z. Lian, J. He, L. Liu, Y. Fan, X. Chen, H. Jiang, *Nat. Commun.* 2023,

617   **14**, 2752.

618 60 Z. Lian, L. Liu, J. He, S. Fan, S. Guo, X. Li, G. Liu, Y. Fan, X. Chen, M.

619   Li, C. Chen, H. Jiang, *Chem. Eur.* 2023, e202303819.

620 61 J. He, Y. Fan, Z. Lian, S. Guo, Y. Wang, H. Jiang, *Adv. Optical Mater.*

621   2023, 2302221.

622 62 J. K. Park, Z. S. Yoon, M.-C. Yoon, K. S. Kim, S. Mori, J.-Y. Shin, A.

623   Osuka, D. Kim, *J. Am. Chem. Soc.* 2008, **130**, 6, 1824-1825.

624 63 Q. Xu, C. Wang, J. He, X. Li, Y. Wang, X. Chen, D. Sun, H. Jiang, *Org.*

625   *Chem. Front.* 2021, **8**, 2970.

626 64 Q. Xu, C. Wang, D. Zheng, J. He, Y. Wang, X. Chen, H. Jiang, *J. Org.*

627   *Chem.* 2021, **86**, 13990-13996.

628 65 Q. Xu, C. Wang, X. Chen, Y. Wang, Z. Shen, H. Jiang, *Org. Chem. Front.*

629   2022, **9**, 4981.

630 66 H. L. Schmider, A. D. Becke, *Chemical content of the kinetic energy*

631   *density, Journal of Molecular Structure: THEOCHEM,* 2000, pp. 51-61.

632 67 J. F. Gonthier, S. N. Steinmann, L. Roch, A. Ruggi, N. Luisier, K. Severin,

633   C. Corminboeuf, *Chem. Commun.* 2012, **48**, 9239-9241.

634 68 Z. Liu, T. Lu, S. Hua, Y. Yu, *J. Phys. Chem. C.* 2019, **123**, 18593−18599.

635 69 K. Kuroda, K. Yazaki, Y. Tanaka, M. Akita, H. Sakai, T. Hasobe, N. V.

636   Tkachenko, M. Yoshizawa, *Angew. Chem. Int. Ed.* 2019, **58**, 1115 –1119.

637 70 K. Kuroda, K. Yazaki, Y. Tanaka, M. Akita, H. Sakai, T. Hasobe, N. V.

638   Tkachenko, M. Yoshizawa, A Pentacene-based Nanotube Displaying

639   Enriched Electrochemical and Photochemical Activities*. Angew. Chem.*

640   *Int. Ed.* 2019, **58**, 1115 –1119.

641

642 SYNOPSIS TOC.

643 All-carbon nanohoops with [4n]Möbius topology via combining

644 [5]helicene and cycloparaphenylene units exhibit bright circularly

645 polarized luminescence and Hückel aromaticity.

646